

1 **Quantitative composition and mesoscale ion distribution in p-type organic mixed ionic-
2 electronic conductors**

4 Ruiheng Wu,^{1,†} Bryan D. Paulsen,^{2,†} Qing Ma,⁴ Iain McCulloch,⁵ Jonathan Rivnay^{2,3*}

6 ¹Department of Chemistry, Northwestern University, Evanston, IL, 60208, USA

7 ²Department of Biomedical Engineering, Northwestern University, Evanston, IL, 60208, USA

8 ³Simpson Querrey Institute, Northwestern University, Chicago, IL, 60611, USA

9 ⁴DND-CAT, Synchrotron Research Center, Northwestern University, Evanston, IL, 60208, USA

10 ⁵Department of Chemistry, University of Oxford, Oxford, OX1 3TA, UK

11 E-mail: jrivnay@northwestern.edu

12 [†] The authors contributed equally to this manuscript

13 Keywords: organic mixed ionic-electronic conductors, X-ray fluorescence, ion composition.

15 **Abstract**

16 Understanding the ionic composition and distribution in organic mixed ionic-electronic conductors
17 (OMIECs) is crucial for understanding their structure-property relationships. Despite this, direct
18 measurements of OMIEC ionic composition and distribution are not common. In this work, we
19 investigate the ionic composition and mesoscopic structure of three typical p-type OMIEC
20 materials: an ethylene glycol treated crosslinked OMIEC with large excess fixed anionic charge
21 (EG/GOPS-PEDOT:PSS), an acid treated OMIEC with tunable fixed anionic charge (crys-
22 PEDOT:PSS), and a single component OMIEC absent any fixed anionic charge (pg2T-TT). A
23 combination of X-ray fluorescence (XRF) and photoelectron spectroscopies (XPS), gravimetry,
24 coulometry, and grazing incidence small angle X-ray scattering (GISAXS) techniques were
25 employed to characterize these OMIECs following electrolyte exposure and electrochemical
26 cycling. In particular, XRF provided quantitative ion-to-monomer compositions for these OMIECs
27 from passive ion uptake following aqueous electrolyte exposure, and potential driven ion
28 uptake/expulsion following electrochemical doping and dedoping. Single ion (cation) transport in
29 EG/GOPS-PEDOT:PSS due to Donnan exclusion was directly confirmed, while despite
30 significant fixed anion concentration in crys-PEDOT:PSS doping and dedoping was shown to

1 occur through mixed anion and cation transport. Controlling the fixed anionic (PSS⁻) charge
2 density in crys-PEDOT:PSS mapped the strength of Donnan exclusion in OMIEC systems
3 following a Donnan-Gibbs model. Anion transport dominated pg2T-TT doping and dedoping, but
4 a surprising degree of anionic charge trapping ($\sim 10^{20}$ cm⁻³) was observed. GISAXS revealed
5 minimal ion segregation both between PEDOT- and PSS-rich domains in EG/GOPS-PEDOT:PSS,
6 and between amorphous and semicrystalline domains in pg2T-TT, but showed significant ion
7 segregation in crys-PEDOT:PSS at length scales of tens of nm, ascribed to inter-nanofibril void
8 space. These results bring new clarity to the ionic composition and distribution of OMIECs that
9 are crucial for accurately connecting structure and properties in these materials.

10

11 **Introduction**

12 Organic mixed ionic-electronic conductors (OMIECs) are π -conjugated soft materials with ionic
13 or ionophilic functionalization that imparts free ion miscibility and transport. OMIEC's ability to
14 both transport and couple ionic and electronic charge make them attractive active materials for
15 next generation bioelectronics,¹⁻⁴ energy storage,⁵ electrochromic,^{6, 7} and neuromorphic
16 computing applications.^{8, 9} There has been a recent growth in characterization work with the aim
17 of unraveling OMIEC structure-property relationships in order to direct synthetic design of
18 OMIECs and improve performance in targeted applications. These efforts are challenging as
19 OMIECs in application relevant conditions are often swollen with ions and solvent, and the
20 resulting electrolyte-swollen structure is sensitive to electrochemical potential and the
21 composition of the surrounding media. While significant advances have improved the
22 understanding of application-relevant structure and electronic transport, significantly less work
23 has explored ionic/solvent composition and transport in OMIECs. This critically limits the
24 development of OMIECs, since understanding the structure property relationships that dictate
25 mixed transport require knowledge of OMIEC composition, especially the concentration and
26 distribution of ionic species.

27 Previous studies of OMIECs have employed electrochemical quartz crystal microbalance
28 (EQCM) to capture mass/thickness changes.¹⁰⁻¹⁴ Microbalance techniques cannot differentiate
29 between species that contribute to thin film mass changes, thus some studies reporting dopant

1 and solvent concentrations depend on the assumption that counter ion contributions are
2 excluded,^{10, 11} though others have found evidence indicating counter ion contributions.^{15, 16}

3 Recent work has employed X-ray photoelectron spectroscopy (XPS) and glow discharge optical
4 emission spectroscopy (GDOES) to quantify the composition of OMIECs.^{9, 16, 17} These studies
5 have monitored the passive (not driven by applied potential) uptake of anion-cation pairs,¹⁷ the
6 competition of cation expulsion and anion injection in the electrochemical p-doping processes,¹⁶
7 and the ion trapping that enables non-volatile electrochemical state retention.⁹ These reports give
8 important insights into the fundamental processes in OMIECs. However, they are hindered by
9 high detection limits and difficulties with calibration that constrain them to reporting qualitative
10 results. Thus, quantitative composition determination in OMIECs remains to be achieved.

11 Additionally, the depth profiling involved in both techniques to probe the composition within the
12 OMIEC samples makes them necessarily destructive techniques. This limits the potential
13 adoption of *in situ*/*operando* implementations of these techniques to capture the dynamic
14 application relevant composition. Finally, due to the diversity and complexity of OMIEC
15 mesoscale structure,¹⁸ composition throughout OMIEC is not expected to be constant (possible
16 ion segregation between amorphous and crystalline domains, and between polyelectrolyte and
17 conjugated polymer domains). Where ions and solvent molecule segregate is as important as how
18 many ions there are. Thus, bulk OMIEC composition determination should be paired with
19 investigations of component distribution.

20 In light of these issues, there is a critical need for quantitative non-destructive *in situ*/*operando*
21 compatible techniques to measure OMIEC ionic composition and distribution. To this end,
22 synchrotron radiation techniques (especially spectroscopy and scattering) present an attractive
23 means of accomplishing both. X-ray fluorescence (XRF) spectroscopy has been performed in a
24 wide range of elemental analyses, known for being fast, non-destructive, accurate, and is ideal
25 for the quantitative analysis of low concentration elements in thin film samples.^{19, 20} Common
26 benchtop XRF instruments often use a fixed incident wavelength, which results in weak
27 fluorescence intensity when the incident photon energy is far from the absorption edge of the
28 target element. In synchrotron light sources, the accuracy of the analysis of the target element at
29 the absorption edge of the element is further improved because of the high brilliance and tunable
30 wavelength of the incident X-rays.²¹ Selection of known composition calibrant samples with

1 similar geometry and elemental ratio to the sample of interest^{22, 23} enables quantitative elemental
2 analysis of OMIEC samples, and has allowed high precision determination of trace impurities in
3 conjugate polymer based solar cells.²⁴

4 Small angle X-ray scattering with synchrotron sources enables the probing of mesoscale
5 structure. Significant work has been carried out to understand OMIEC as-cast structure,
6 revealing the effect of additives and processing conditions on mesoscale structure,²⁵⁻²⁷ and
7 mesoscale domain formation during film deposition.^{28, 29} Specifically, the mesoscale morphology
8 of polymer blends is remarkably affected by molecular chemical doping by the interaction
9 between the ionic dopants and the polymer chains.^{30, 31} While in situ work has been reported on
10 the electrochemical potential mesoscale structure in Li⁺ transporting block copolymers for
11 battery applications,^{32, 33} there have been a noted absence of work reporting small angle
12 scattering in other types of OMIECs subjected to the electrochemical doping and dedoping
13 occurring in application relevant conditions.

14 Here we report ex situ XRF and grazing incidence X-ray scattering studies of two prototypical p-
15 type OMIECs: poly(3,4-ethylenedioxythiophene) polystyrene sulfonate (PEDOT:PSS), a dual
16 component OMIEC consisting of a conjugated polymer templated on a polyelectrolyte; and
17 pg2T-TT a single component conjugated polymer electrolyte OMIEC. For both we explore the
18 OMIEC ion composition when the thin films are exposed to electrolytes, and at various
19 electrochemical potentials (dedoped, naturally doped, redoped to a higher oxidation level)
20 relating to degree of oxidation across systematically varied electrolyte concentration and pH. The
21 quantitative determination of the potential/concentration/pH dependent OMIEC composition
22 reveals the role of buffering and Donnan exclusion in polyelectrolyte based OMIECs containing
23 an excess of fixed ionic charge. Additionally, massive amounts of ionic charge trapping
24 compensated by trapped localized electronic charge is revealed in conjugated polymer
25 electrolytes lacking fixed ionic charge. These synchrotron-based ex situ XRF measurements
26 were complemented with benchtop XRF, XPS, and EQCM studies. Further, investigating the
27 composition of record high conductivity acid crystallized PEDOT:PSS (crys-PEDOT:PSS)
28 reveals the limits of Donnan exclusion and the complex composition that accompanies peak
29 OMIEC conductivity.

1 To investigate the ion distribution ex situ, grazing incidence small angle X-ray scattering
2 (GISAXS) was carried out for both the prototypical systems and record performing crys-
3 PEDOT:PSS. The contrast of GISAXS patterns provides the homogeneity information of the
4 organic film at mesoscale and gives insight into the distribution of ions at different doping levels.
5 These results represent the first quantitative compositional determination of OMIEC ion
6 distribution during electrochemical cycling and establish quantitative techniques necessary to
7 produce meaningful structure-property relationships to drive the rational design of next-
8 generation OMIECs.

9

10 **Experimental Session**

11 **Sample preparation:** PEDOT:PSS (Clevios PH-1000), purchased from Heraeus Holding
12 GmbH, was filtered through 0.45 μm PES filters to remove large particles. For EG/GOPS-
13 PEDOT:PSS samples, the filtrate was mixed with 5% EG, 1% GOPS and 0.1% DBSA. The
14 mixture was spin coated on Kapton for 3000rpm and soft baked at 80°C, followed by another
15 two 1000rpm spin coating to achieve a 3-layer film (thickness \sim 300nm). The samples were
16 annealed at 140°C for 30 minutes. To increase the film thickness for a better signal-to-noise
17 ratio, we have implemented a drop-casting method for the crys-PEDOT:PSS and pg2T-TT
18 samples. This approach was chosen as these materials are not well-suited for multilayer spin
19 coating. For crys-PEDOT:PSS, the filtrate was directly drop-casted on degenerately p-doped Si
20 wafer (0.001-0.005 ohm cm⁻¹) (University Wafer) at 70°C that had been successively sonicated
21 in acetone and isopropyl alcohol, and exposed with UV-ozone prior to drop-casting. All the
22 samples were dried at 120°C for 30 minutes. After cooling down, the samples were treated with
23 sulfuric acid (Sigma) of different concentration for 3 hours. After rinsing to pH neutral, the
24 samples were first heated at 60°C for 30 minutes and then 120°C for 30 minutes in ambient to
25 form homogenous purple films. For pg2T-TT samples, the solid state pg2T-TT was dissolved in
26 chloroform (1mg/mL) and heat at 45°C overnight. The solution was drop-casted on Kapton
27 inside a chloroform vapor saturated chamber.

28 **X-ray Fluorescence measurement:** The XRF measurements were carried out in fluorescence
29 mode using the spectroscopy-grade ionization chambers (FMB-Oxford). The X-ray beam size on
30 the sample is 1.0 \times 6.0 (V \times H) mm. The spectra with excitation energy before (15000 eV) and

1 after (15250 eV) Rb K edge were collected to decouple the overlapping Br K_β and Rb K_α peaks.
2 Benchtop XRF measurements were carried out in vacuum using the Xenemetrix energy
3 dispersive x-ray fluorescence (ED-XRF) analyzer. The sample size is 1.0 x 1.0 inch and the
4 footprint of the X-ray beam on the sample is a circle with a radius of 0.75 inches. The excitation
5 X-ray energy was selected at 20keV to properly excite the element of interest. Ti filter was used
6 to remove noise signal over 5keV (for Rb and Br peaks). The integration time for each spectrum
7 was 5 minutes and blank polymer film was used for background deduction over 2.4keV (higher
8 than the S peak). All data analysis was performed with Matlab software.

9 **X-ray Photoelectron Spectroscopy measurement:** The XPS spectra were taken using Thermo
10 Scientific ESCALAB 250Xi equipped with a monochromatic KR Al X-ray source (spot size of
11 900 μ m) at the Northwestern University Atomic and Nanoscale Characterization Experimental
12 center (NUANCE). Before data collection, a flood gun was used for charge compensation. The S
13 peak was measured without ionic etching to avoid the reduction of sulfonate. The salt ion peaks
14 (Na, Cl, Br and Rb) were measured after 30s ionic beam etching (~100nm) to avoid the surface
15 contamination. The curve fitting was performed using the Avantage (Thermo Scientific)
16 software.

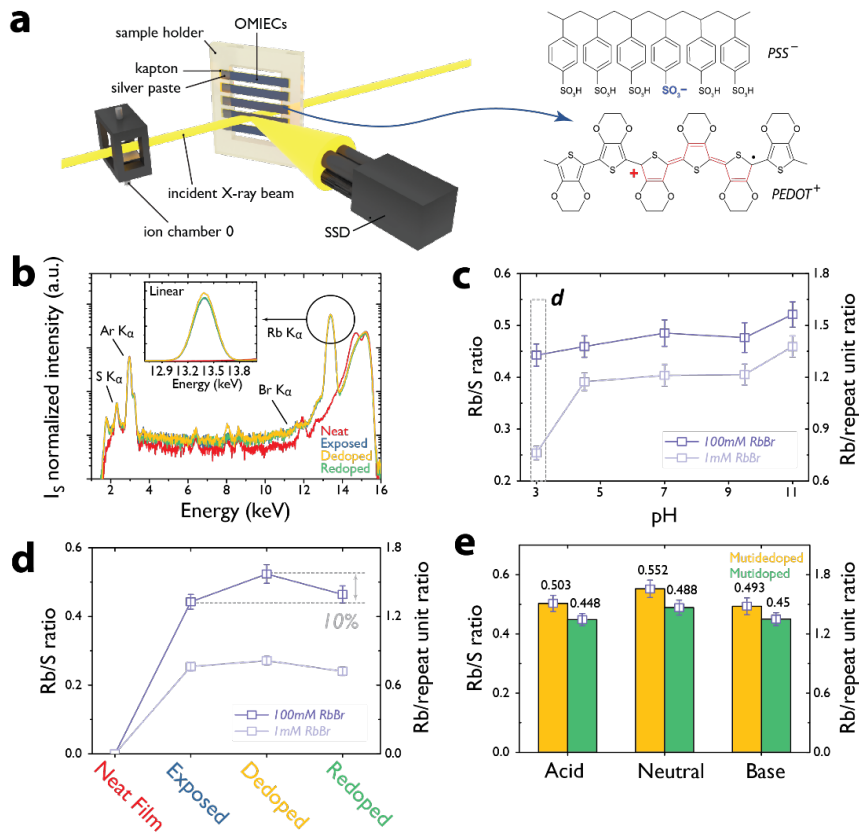
17 **GISAXS measurement:** GISAXS measurements were performed at beamline 8-ID-E of the
18 Advanced Photon Source, Argonne National Laboratory with the incident energy of 10.92 keV at
19 an incident angle of 0.14°. The samples were under vacuum at room temperature, with images
20 collected by a Pilatus 1MF pixel array detector 2.185 m away from the sample. The samples for
21 GISAXS were prepared by: spin-coating and drying (pristine); spin-coating, drying, exposing to
22 electrolyte for 30 min, rinsing in DI water for three times and drying (exposed); spin-coating,
23 drying, exposing to electrolyte for 30 min, cycling at different voltage level (for EG/GOPS-
24 PEDOT:PSS, we de-doped at -0.6V vs Ag/AgCl and re-doped at 0.1V vs Ag/AgCl; for crys-
25 PEDOT:PSS, we de-doped at -0.6V vs Ag/AgCl and re-doped at 0.6V vs Ag/AgCl; for pg2T-TT,
26 we doped at 0.5V vs Ag/AgCl and de-doped at -0.2V vs Ag/AgCl), rinsing in DI water for three
27 times and drying. Data were processed with MATLAB, Irena, Nika, and Indra SAXS Igor code.

28

29 **Results and Discussion**

1 To measure elemental composition, ex situ XRF (**Figure 1a**) and XPS were performed on
 2 OMIECs exposed to and electrochemically cycled in aqueous electrolyte. Due to the limited path
 3 length of photoexcited electrons, XPS is only sensitive to the sample surface. However, XRF has
 4 a bulk sensitivity (micron scale), which provides bulk compositional information in a non-
 5 destructive and fast manner.

6 Metal halide salts were prioritized as they better reflect the ions present in biotic environments.
 7 In particular, RbBr was chosen as both the anion and cation fluoresce at higher energy (>12 keV)
 8 avoiding fluorescence overlap from ambient Ar (**Figure 1b**) and excessive photon absorption,
 9 which allows XRF measurements to be carried out under ambient conditions. These
 10 considerations are especially important when looking towards future in-situ/operando application
 11 of XRF measurements. In evaluating the generality of monovalent metal halide salts, OECTs
 12 employing aqueous 100 mM RbBr performed nearly identically to the more commonly
 13 employed NaCl electrolytes at equivalent concentrations.³⁴ In addition, XPS performed on both
 14 RbBr and NaCl exposed samples revealed similar ion uptake, implying RbBr as a suitable
 15 approximation of other monovalent metal halide salts (**Figure S1**).



1 **Figure 1** a) ex situ XRF setup and the structure of model OMIEC material, PEDOT:PSS; b)
2 XRF spectra for EG/GOPS-PEDOT:PSS exposed and electrochemical cycled in 100mM at
3 pH=7; c) Rb/S elemental ratio for EG/GOPS-PEDOT:PSS exposed to 1mM and 100mM RbBr
4 aqueous electrolytes of different pH; d) Rb/S elemental ratio for EG/GOPS-PEDOT:PSS in
5 different doping level electrochemical cycling in 1mM and 100mM at pH=3; e) Rb/S elemental
6 ratio for EG/GOPS-PEDOT:PSS after multiple electrochemical cycling in acid (pH=3), neutral
7 (pH=7) and basic (pH=11) conditions.

8

9 Compositional calibration curves were established by measuring the XRF spectra of a series of
10 thiourea/RbBr mixture films with known S, Rb, and Br composition (**Figure S2a**). Calibration
11 samples were spin coated on the same substrates as the OMIEC samples to avoid introducing
12 new fluorescence that would complicate comparisons. Using these calibration data, XRF peak
13 area ratios were converted into quantitative elemental compositions (**Figure S2b**).

14 First investigated was the benchmark OMIEC, PEDOT:PSS (structure in **Figure 1a**), prepared
15 and cast using a commonly reported recipe containing ethylene glycol (EG) and (3-
16 glycidyloxypropyl)trimethoxysilane (GOPS). EG functions as a processing additive known to
17 drive PEDOT and PSS phase segregation yielding a morphology conducive to electronic
18 transport,^{26, 35-37} while GOPS is used as a crosslinker, activated by an ambient “hard-bake”, to
19 impart stability to the thin film and prevent film delamination or redispersion.^{38, 39} The
20 PEDOT:PSS itself consists of a water suspension of PEDOT templated upon an excess of PSS. A
21 fraction of PSS⁻ anions serve as dopants, stabilizing positive charge carriers (holes) on the
22 PEDOT backbone. Excess PSS⁻ anions are charge balanced with protons or cations. As supplied,
23 the commercial PEDOT:PSS employed was in the acid form (PSSH) with protons
24 counterbalancing the remaining excess PSS⁻.

25 The PEDOT:PSS water suspension was blended with 5% EG, 1% GOPS and 0.1%
26 dodecylbenzenesulfonic acid (DBSA). The suspension was spin coated on Kapton films that
27 were precleaned with acetone and iso-propanol. As cast EG/GOPS-PEDOT:PSS films contained
28 a 1:2.0 thiophene sulfur to sulfonate sulfur ratio (as determined by XPS, see **Figure S1a&d**), in
29 line with previous reports (1: 2.2-2.5).^{10, 40} Considering that PEDOT:PSS prefers a doped state

1 with a hole density of approximately one hole per three ethylenedioxothiophene (EDOT) repeat
2 units,⁴¹⁻⁴⁴ roughly 83% of the sulfonates are excess, not functioning as dopants.

3 Ex situ XRF revealed that when exposed to RbBr electrolyte, EG/GOPS-PEDOT:PSS films
4 underwent a large proton-cation exchange, with Rb⁺ supplanting H⁺ within the film. The
5 equilibrium between proton and cation counterbalancing excess sulfonates was weakly
6 dependent on electrolyte concentration and pH, showing significant differences only at the pH
7 extremes and low metal halide concentration (**Figure 1c**). Thus, PSS⁻ functioned as a buffer,
8 minimizing the effect of electrolyte concentration and pH on OMIEC composition, except for
9 high pH (11) conditions and the combined low pH (3) low salt concentration (1 mM RbBr)
10 condition. In the initially exposed low pH (3) and low salt concentration (1 mM RbBr)
11 conditions, where electrolyte proton and Rb⁺ concentrations are equivalent, there is likely equal
12 parts Rb⁺ and protons within the film. For neutral electrolyte solutions near biologically relevant
13 salt concentrations (100 mM), the Rb⁺ concentration within the film effectively supplants the
14 entire disassociated proton concentration.

15 Initial cycles for some pH and electrolyte concentration conditions presented smaller than
16 expected modulation of the cation concentrations, indicating a significant role of proton transport
17 in initial film doping and dedoping. However, repetitive cycling appeared to break in the films
18 and drive them towards a reversible equilibrium with the electrolyte that was dominated by metal
19 cation transport. These multiple cycling experiments revealed a stabilized ~10% difference in
20 Rb⁺ concentration between the doped (0 V vs Ag/AgCl) and dedoped (-0.6 V vs Ag/AgCl) states
21 (**Figure 1d**) across different pHs. While -0.6 V vs Ag/AgCl is not rigorously dedoped (zero
22 electronic charge carrier density), it is sufficient to recover the majority of the neutral PEDOT
23 species and arrive at the dedoped microstructure.⁴⁵ Potentials necessary to drive PEDOT:PSS to
24 the fully neutral state result in significant faradaic currents due to electrolyte breakdown or
25 polymer degradation,^{10, 46-48} and thus were avoided. When cycling from 0 to -0.6 V vs Ag/AgCl,
26 for the neutral 100 mM RbBr condition, this represents a modulation of ~0.2 Rb⁺ per
27 ethylenedioxothiophene (EDOT) repeat unit. Given the presumed total doped hole density of
28 ~0.33, this indicated much of the modulation in hole density is achieved through modulation of
29 Rb⁺ dopant density, though some minority proton contribution cannot be ruled out. The cation
30 composition is reversible during multiple cycles of charging and discharging (**Figure 1e**). The

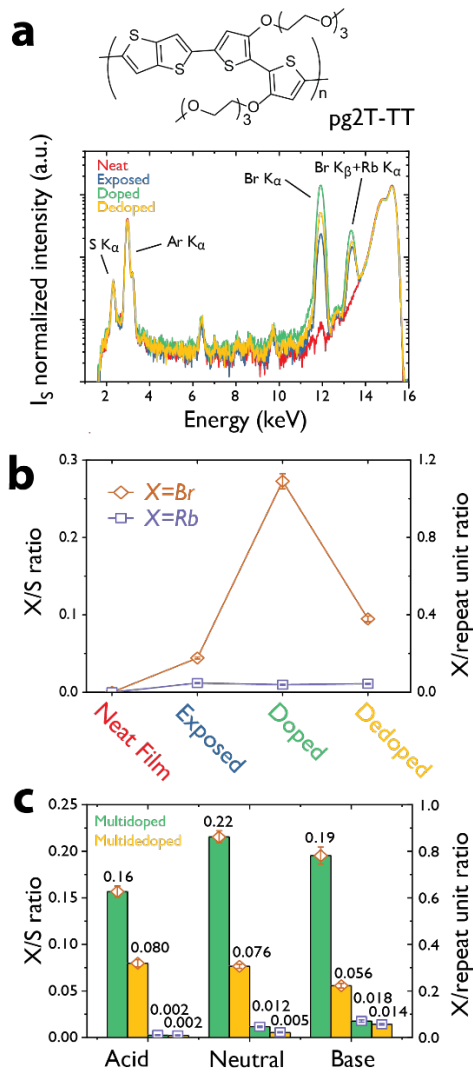
1 Rb/S ratio increased slightly to 0.55 after multiple cycles in the dedoped state and 0.49 in the
2 doped state.

3 Across electrolyte concentration and pH, Br⁻ anions were rigorously excluded to levels below the
4 detection limit (<0.001 Br⁻ per EDOT repeat unit) due to Donnan exclusion arising from the
5 fixed anionic charge of the excess PSS polyelectrolyte. This empirically validates the
6 assumptions no mobile anion contribution implicit to previous PEDOT:PSS EQCM studies.^{10, 38,}
7 ^{49, 50} However, in previous works the cation concentration was not measured directly but
8 calculated from the charging currents, thus any faradaic side reactions not contributing to hole
9 carrier density undermined the accuracy of the derived cation concentration within the OMIEC
10 film.

11 To attend to this complication, EQCM was carried out to compliment these XRF studies and
12 allow a complete mass and charge balance of the OMIEC films. Assuming a density of 1.0g/cm³
13 and knowing the modulated cation concentration through XRF, the contribution to the mass
14 change due to uptake of water molecules was calculated. The number of cations
15 (injected/expelled) during cycling as quantified by XRF (**Figure 1e**) was used in the mass
16 balance quantified by EQCM (**Figure S3a**) to calculate the amount of water that accompanies
17 cation (injected/expelled). The combined experiments here indicate that on average ~11.6 H₂O
18 molecules accompany each Na⁺ cation injected/expelled in to EG/GOPS-PEDOT:PSS. This is
19 nearly three times the estimated accompanying water molecules previously reported using solely
20 EQCM methods where the cation flux was equated with measured electrical current. This
21 highlights the overestimate of cation content that can occur when measured currents are assumed
22 to be purely cation flux. This ignores faradaic reactions that result in direct charge transfer,
23 which can be especially large in aqueous environments in the presence of oxygen.^{51, 52} These
24 faradaic reactions arising from PEDOT based materials can in fact be harnessed as reported in
25 PEDOT-based electrocatalysts.^{51, 53-55}

26 Our calculated cation-associated water content is more in line with near ambient pressure XPS
27 measurements of water content (~8-10 per cation) associated with a metal halide
28 counterbalanced PSS⁻ functional group.⁵⁶ It is intuitively reasonable that our cation-associated
29 water uptake of a PSS containing film in contact with liquid electrolyte would exceed sorption
30 measurements of PSS films in 100% relative humidity environments (but not in contact with

1 liquid water). The experiments reported here indicate that cation transport into the film is
2 accompanied by more than a single hydration shell of ~6 water molecules.^{57, 58}



4 **Figure 2** a) XRF spectra for pg2T-TT exposed and electrochemical cycled in 100mM at pH=7;
 5 b) Br (brown diamond) and Rb (violet square) to S ratio of pg2T-TT in different electrochemical
 6 doping level; c) Rb (brown diamond) or Br (violet square) to S elemental ratio for pg2T-TT after
 7 multiple electrochemical cycling (the doped states filled with green and the dedoped states filled
 8 with yellow) in acid (pH=3), neutral (pH=7) and basic (pH=11) conditions.

10 While EG/GOPS-PEDOT:PSS is a prototypical conjugated polymer/polyelectrolyte composite
11 OMIEC, polythiophenes with oligoethylene glycol side chains have become increasingly popular

1 conjugated polymer electrolyte OMIECs.⁵⁹⁻⁶¹ In particular, pg2T-TT (**Figure 2a**) has been
2 investigated for a variety of applications.^{17, 59, 62, 63} Lacking any fixed ionic charge, Donnan
3 exclusion is not expected in pg2T-TT, and both cations and anions appeared in the XRF spectra
4 (**Figure 2a&b**). The florescence spectra at 200eV below the Rb absorption edge were collected
5 to deconvolute and Rb K_α peaks from the overlapped Br K_β peaks (**Figure S4a**). XRF following
6 electrolyte exposure revealed the passive uptake of both anions and cations, 0.16 Br⁻ and 0.04
7 Rb⁺ per repeat unit (**Figure 2b**). This was in agreement with previous qualitative measurements
8 of ion uptake in contact with ionic liquid electrolytes.¹⁷ However, here the calibrated quantitative
9 measure of individual ion concentrations revealed that anions and cations did not uptake in equal
10 amount, indicating extensive passive doping of pg2T-TT. This is attributed to its relatively
11 shallow HOMO allowing for rather efficient doping via ambient oxygen.⁵¹ The passive uptake of
12 Rb⁺ led to a cation concentration that subtly varied with doping (oxidation) state.

13 Initial cycling between the doped state (+0.5V vs Ag/AgCl) and dedoped state (-0.2V vs
14 Ag/AgCl) greatly modulated the Br⁻ anion concentration, though even when a reductive
15 electrochemical potential was applied a large excess of anions (uncompensated by cations)
16 remained. Unlike the PEDOT:PSS cycling, it should be noted here that the reductive potentials
17 applied were sufficient to fully dedope the polymer. These initial phenomena persisted upon
18 multiple cycles, equilibrating to seemingly permanent presence of 0.021 charged balanced anions
19 and cations per repeat unit, and a further uncompensated 0.29 excess anions per repeat unit
20 (**Figure 2c** and the second right column in **Figure S4b**). Due to the energetic favorability of
21 charge neutrality, these seemingly uncompensated excess anions are presumably
22 counterbalanced by localized positive charge on the polymer backbone (i.e. trapped electronic
23 charge). This measured trapping level ($\sim 10^{20}$ cm⁻³) is much higher than expected defect levels in
24 polythiophenes ($10^{13} - 10^{19}$ cm⁻³).⁶⁴⁻⁶⁹ Thus it is surmised that electrochemical cycling of the
25 films does not simply passivate existing trapped electronic charge with excess anions, but
26 induces many additional trap sites as well.

27 From the dedoped to doped state the concentration of charge balanced anions and cations
28 roughly doubled to 0.048 anion-cation pairs per repeat unit, and the concentration of
29 uncompensated anion dopants nearly tripled to 0.82 per repeat unit (the second left column in
30 **Figure S4b**). The presence of charged balanced ions appears to represent a permanent population

1 due to passive electrolyte swelling of the film. The increase in charge balanced anion-cation
2 pairs in the doped state reflects an increase miscibility of the polymer and electrolyte when the
3 polymer is charged.

4 Interestingly, excess cation accumulation in the dedoped state was not observed. Instead, cation
5 composition in the dedoped state was diminished compared to the doped state. This stood in
6 contrast to previous reports where a dedoping occurs by both anion expulsion and cation
7 insertion to counterbalance remaining anion dopants in both conjugated¹⁶ and radical OMIECs.¹⁵
8 It must be noted that these previous studies either did not employ metal halide salts, or in the
9 case of radical polymers, employed non-aqueous electrolytes. The absence of cation
10 accumulation highlights that aqueous metal halide transport in OMIEC based bioelectronic
11 devices can deviate significantly from systems employing salts and solvents more common in
12 energy storage devices. Here, cations do not contribute to the doping/dedoping process, but
13 simply participate through passive electrolyte swelling of the pg2T-TT film, the miscibility of
14 which depends on the film's charged state.

15 Lacking any excess polyelectrolyte to act as a buffer (such as in the case of PEDOT:PSS), the
16 ion composition of pg2T-TT was found to be dependent on electrolyte concentration and pH
17 (**Figure S5**). At neutral pH, anion concentration in the polymer was positively correlated with
18 electrolyte concentration at all states (exposed/doped/dedoped). The observed dependence of
19 anion concentration in the polymer upon electrolyte concentration was larger than would be
20 expected from a shift in doping state due to a Nernst-like shift in electrochemical potential (59
21 mV shift per decade of electrolyte concentration). Instead, a ~55% drop in dopant anion
22 concentration was observed when decreasing electrolyte concentration from 100 to 10 mM, and a
23 further ~40% drop from 10 to 1 mM (**Figure S5a**). The persistent (trapped) anion concentration
24 within the rigorously dedoped film was also dependent on electrolyte concentration. The trapped
25 anions were in an apparent equilibrium with the contacting aqueous electrolyte, undergoing a 30-
26 40% decrease with each ten-fold decrease in electrolyte concentration (**Figure S5a**).

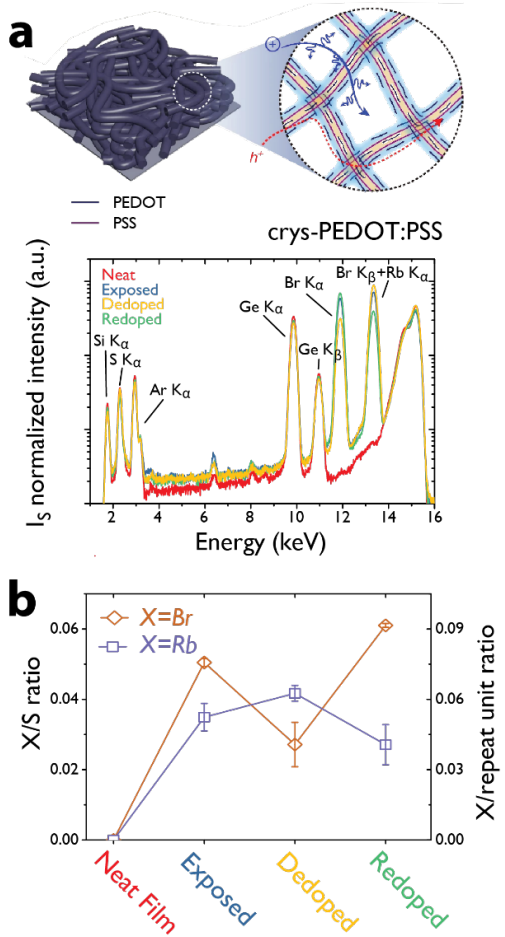
27 Cation concentration was positively correlated with pH, rising from 0.008 (0.008) Rb⁺ per repeat
28 unit in acidic conditions to 0.072 (0.056) Rb⁺ per repeat unit in basic conditions in the doped
29 (dedoped) state (**Figure S4b**). This reflects the competition in acidic solution between the Rb⁺
30 and proton counterbalancing the halide anion, and in the case of basic solutions,

1 counterbalancing the hydroxide anion. The trapped anion concentration shows an opposite trend
2 with pH, falling from 0.31 trapped excess Br⁻ per repeat unit in acidic conditions to 0.16 trapped
3 excess Br⁻ per repeat unit in basic conditions (**Figure S4b**). This likely reflects the effect of
4 protonation of the polymer on both free carrier and defect/trap density.⁷⁰⁻⁷³

5 The modulated Br⁻ concentration (difference between doped and dedoped state) was nominally
6 identical in neutral and basic conditions (0.53 and 0.54 Br⁻ dopants per repeat unit, respectively,
7 see **Figure S4b**). This indicated that basic pH seemed not to effect the doping/dedoping process.
8 However, the acid condition displayed a diminished degree of Br⁻ dopant modulation of only
9 0.31 Br⁻ dopants per repeat unit, indicating the protonation of thiophene rings may disrupt the
10 doping/dedoping process.⁷⁰

11 Summarizing the contrast between EG/GOPS-PEDOT:PSS and pg2T-TT, EG/GOPS-
12 PEDOT:PSS undergoes an initial exchange of protons in the film with metal cations from the
13 electrolyte. The excess polyelectrolyte in EG/GOPS-PEDOT:PSS simplifies the composition
14 situation by Donnan excluding uptake of mobile anions and buffering the film against pH and
15 electrolyte concentration, such that doping/dedoping involves a fairly consistent modulation
16 of >0.2 cations per EDOT repeat unit. However, this cation modulation brings with it a large flux
17 of water molecules in/out of the film. Conversely, pg2T-TT undergoes passive electrolyte uptake
18 (water and anion-cation pairs) and passive doping. Electrochemical cycling accumulates a
19 remarkably high concentration of excess anions that apparently balance/trap electronic charge in
20 the polymer. Lacking fixed charge, pg2T-TT is unbuffered, and the resulting film composition is
21 highly sensitive to electrolyte concentration and pH.

22 Having quantified the ion composition of prototypical polyelectrolyte:conjugated polymer and
23 conjugated polymer electrolyte OMIECs, we turned to the top performing OMIEC, sulfuric acid
24 crystallized PEDOT:PSS (crys-PEDOT:PSS).^{74, 75} Post treatment of PEDOT:PSS films with
25 concentrated sulfuric acid removes excess PSS and drives the nanofibrillar crystallization of the
26 remaining PEDOT:PSS.⁷⁶ Treatment with 95% sulfuric acid reduces the PSS-to-PEDOT ratio
27 from ~2:1 to 0.41:1, **Figure S6**, in line with previous reports.⁷⁵⁻⁷⁷



2 **Figure 3** a) XRF spectra for crys-PEDOT:PSS (PEDOT:PSS treated with 95% sulfuric acid)
3 exposed and electrochemical cycled in 100mM at pH=7; Adapted with permission from [⁷⁵]
4 under the terms of the Creative Commons CC BY license. Copyright 2018 Springer Nature. b)
5 Br (brown diamond) and Rb (violet square) to S ratio of 95% sulfuric acid crys-PEDOT:PSS in
6 different electrochemical doping level.

7
8 We have previously reported the XRF determined composition of 95% sulfuric acid crys-
9 PEDOT:PSS in the doped and dedoped states (**Figure 3**).³⁴ Quantitative comparison of crys-
10 PEDOT composition with EG/GOPS-PEDOT:PSS and pg2T-TT are complicated due to
11 substrate effects (thickness dependent Si absorption of S fluorescence leading to likely
12 underestimate of relative Rb and Br concentrations). Qualitatively, crys-PEDOT:PSS exposed,
13 doped, and dedoped composition is radically different from EG/GOPS-PEDOT:PSS as the
14 removal of excess PSS during acid treatment suppresses the effect of Donnan exclusion (**Figure**

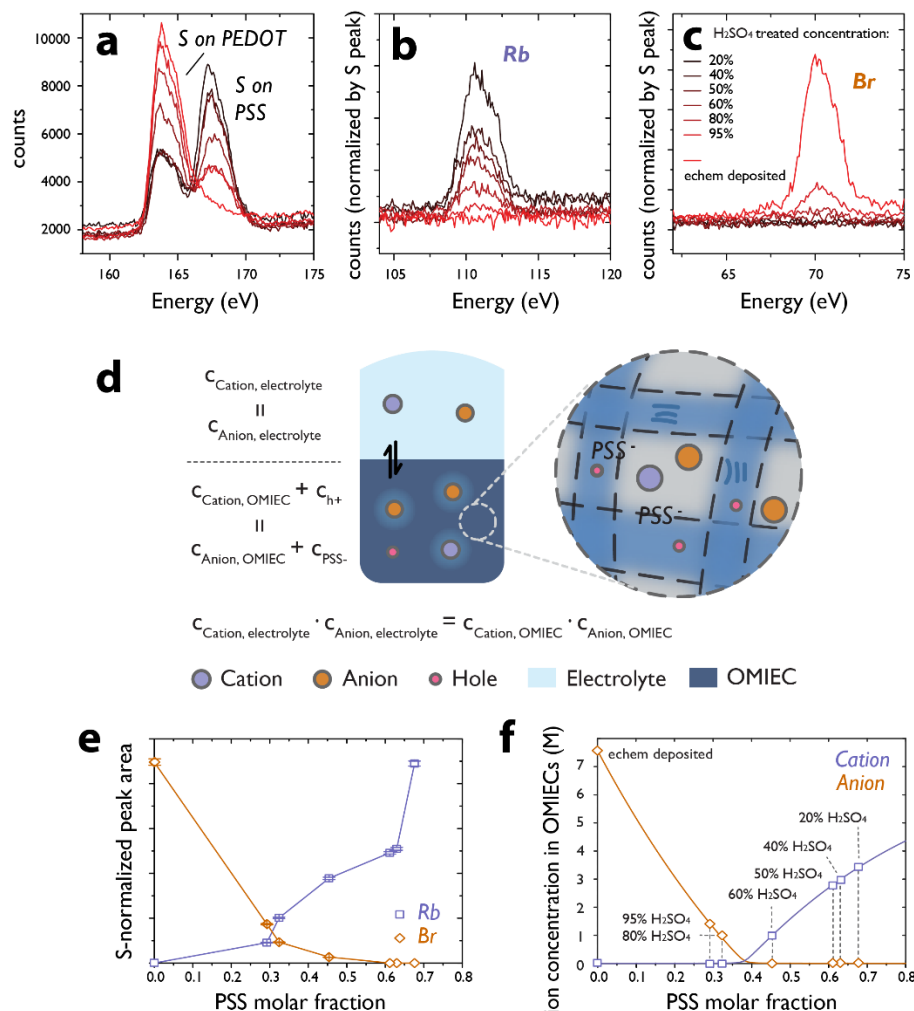
1 3a). Thus, both cations and anions are free to transport in and out the film, and resulting Br-
2 concentrations are on the same order as Rb⁺ concentrations.

3 Electrolyte exposure results in the uptake of both anions and cations, with anions in the excess.
4 Whereas, EG/GOPS-PEDOT:PSS displayed solely Rb⁺ uptake representing proton-cation
5 exchange. In 95% sulfuric acid treated crys-PEDOT:PSS initial proton concentration is minimal
6 as effectively all PSS sulfonates are dopants counterbalancing positive electronic charge on
7 PEDOT, thus no significant proton-cation exchange occurs upon exposure. Instead, in the
8 absence of Donnan exclusion charge balanced anions and cations diffuse into the film (**Figure**
9 **3b**). Further, excess anions accumulate as the equilibrium doping level in neutral aqueous
10 environments is higher than in the sulfuric acid processing conditions, resulting in an ~30%
11 excess of Br⁻ with respect to Rb⁺.

12 When electrochemically dedoped (-0.6 V vs Ag/AgCl), the electronic charge density on the
13 PEDOT is decreased both through the removal of mobile Br⁻ dopants, and the accumulation of
14 excess Rb⁺ cations that counterbalance fixed PSS- dopants, supplanting positive electronic
15 charge (**Figure 3b**). The resulting dedoped composition has a ~37% excess Rb⁺ with respect to
16 Br⁻. Finally, when electrochemically redoped back to a high oxidation state (+0.6 V vs
17 Ag/AgCl), the Br⁻ concentration climbs and the Rb⁺ concentration drops (**Figure 3b**). The
18 resulting redoped composition has a ~55% excess Br⁻ with respect to Rb⁺, with the excess Br⁻
19 functioning as dopants, stabilizing positive electronic charge on PEDOT.

20 The difference in ion uptake between EG/GOPS-PEDOT:PSS and crys-PEDOT:PSS was also
21 reflected in the EQCM data (**Figure S3b**). EG/GOPS-PEDOT:PSS displayed mass uptake during
22 dedoping to a low oxidation state (-0.7 V vs Ag/AgCl) and mass decrease when doping to a high
23 oxidation state (+0.5 V vs Ag/AgCl) with respect to the equilibrium oxidation state (~0.1 V vs
24 Ag/AgCl), consistent with solely cation transport. In comparison, crys-PEDOT:PSS shows a
25 mass increase both upon dedoping and doping to the low (-0.7 V vs Ag/AgCl) and high
26 oxidation states (+0.5 V vs Ag/AgCl), respectively, indicating a more complicated transport
27 environment with both mobile anions and cations contributing. Normalizing the EQCM mass
28 changes by film thickness it becomes apparent that the mass increase (+14%) accompanying
29 dedoping to a low oxidation state (-0.7 V vs Ag/AgCl) and mass decrease (-11-12%)
30 accompanying redoping to the equilibrium oxidation state (~0.1 V vs Ag/AgCl), were nearly

1 identical for both EG/GOPS-PEDOT:PSS and crys-PEDOT:PSS. When further doping to a high
 2 oxidation state (+0.5 V vs Ag/AgCl), crys-PEDOT:PSS displayed a 3.4% mass increase,
 3 compared with 8.3% mass decrease in EG/GOPS-PEDOT:PSS.
 4 Considering crys-PEDOT:PSS ion concentration changes alone, upon doping to a high oxidation
 5 state (large anion concentration increase, moderate cation concentration decrease), a mass
 6 increase is expected (opposite to EG/GOPS-PEDOT:PSS, large cation decreases only) and is
 7 observed with EQCM. Though considering crys-PEDOT:PSS ion concentration changes alone
 8 upon dedoping to a low oxidation state (large anion concentration decrease, moderate cation
 9 concentration increase), a slight mass decrease would be expected. Instead, a moderate mass
 10 increase was observed indicating enhanced water uptake accounting for this discrepancy. Thus,
 11 the amount of water accompanying ion transport cannot be presumed to be constant across
 12 oxidation state.



1 **Figure 4** XPS result of the a) sulfur, b) sulfur normalized rubidium and c) sulfur normalized
2 bromine peaks in PEDOT:PSS treated with sulfuric acid of different concentration (from 20%-
3 95%, black to dark red) and electrochemically deposited PEDOT (red); d) diagram for the
4 Donnan model; e) ion peak fits extracted from the XPS experimental result; f) the calculated
5 result from the Donnan model, plotted with the PSS molar content of each material.

6

7 In sulfuric acid treated crys-PEDOT:PSS, the strength of acid during crystallization allows the
8 control of the excess PSS^- concentration, i.e. allows the tuning of fixed cationic charge within the
9 OMIEC. Leveraging this, we investigated the effect of fixed charge upon ion uptake with XPS
10 compositional analysis on electrolyte exposed PEDOT:PSS previously treated with sulfuric acid
11 of different concentration (**Figure S6**). XPS allowed the simultaneous measure of the
12 PSS:PEDOT ratio and the qualitative ion concentration changes, while XRF was carried out to
13 confirm the ion concentration trends through the bulk.

14 The ratio of sulfonate to thiophene sulfur in the acid treated PEDOT:PSS decreased from 2.08:1
15 to 0.41:1 as the acid treatment concentration increased from 20% to 95% sulfuric acid (**Figure**
16 **4a**). This reflected a modulation of PSS content from 0.68 down to 0.29 PSS mol fraction (with
17 respect to combined PSS and PEDOT content). Electrochemical deposited PEDOT film (soaked
18 in 100mM RbBr solution for ion exchange) was used as a PSS-free (0.0 PSS mol fraction)
19 standard, lacking any fixed cationic charge.

20 XPS revealed the concentration of cations in the polymer films to continually decrease with
21 decreasing PSS mol fraction, with no Rb^+ cations present in the 0.0 PSS mol fraction
22 electrodeposited PEDOT film (**Figure 4b**). The presence of Br^- anions decreased with increasing
23 PSS mol fraction and was suppressed to concentrations below the detection limit above 0.6 PSS
24 mol fraction (>50% sulfuric acid treatment concentration, **Figure 4c**), representing the threshold
25 beyond which fixed cationic charge density was sufficient to exclude mobile anions. These
26 trends were further confirmed with benchtop XRF measurements (**Figure S7a&b**), with some
27 variation in Rb^+ concentration at high PSS mol fraction.

28 A Donnan model was established to semi-quantify the trend of passive ion uptake in different
29 polyelectrolyte (PSS^-) content (see **SI: Gibbs-Donnan Model in PEDOT:PSS**). Shown in

1 **Figure 4d**, the whole system was simplified as two phases: aqueous electrolyte with only mobile
2 anion/cations and OMIECs with extra fixed charges (holes and PSS^-) on the crystalline fiber. Ion
3 concentration inside the OMIEC can be described by the following Donnan-Gibbs equation:

4 $c_{\text{cation,OMIEC}} \cdot c_{\text{Anion,OMIEC}} = c_s^2 \quad (1)$

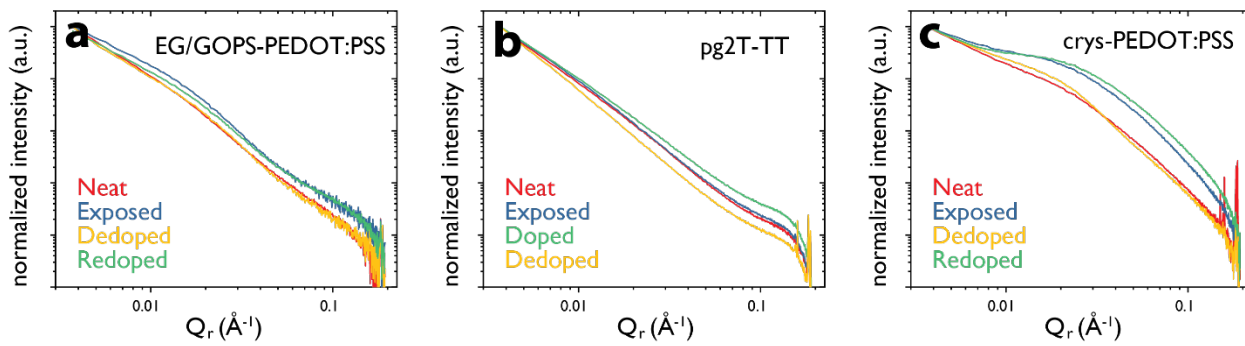
5 Where $c_{X,OMIEC}$ represents the ion concentration in OMIEC and c_s represents the ion
6 concentration in aqueous electrolyte. By assuming a suitable hole concentration,^{44, 76, 77} the
7 specific ion concentration in OMIEC can be solved by combining the charge-neutral condition
8 with the Donnan-Gibbs equation (**Equation 1**, also **S8**), shown in **Figure 4e**. Despite the
9 simplicity of the model, the ion concentrations extracted from XPS (**Figure 4f**) and XRF (**Figure**
10 **S7c**) were in good agreement with the prediction from the Donnan model, capturing the
11 suppression of Br concentration above an intermediate PSS mol fraction (Donnan exclusion of
12 anions). While the exact value of this PSS mol fraction threshold for complete Donnan exclusion
13 in the model was sensitive to assumed hole concentration, the crossover of cation concentration
14 overtaking anion concentration occurs in both the model and the measured data just above a 0.3
15 mol fraction PSS content.

16 As this model only considers the Donnan equilibrium of salt ions between the two phases, it does
17 not account for the evolution of film morphology with increasing acid treatment concentration.
18 With concentrated sulfuric acid treatment, the resulting nano fibrillar structure introduces void
19 space within the film, where charge balanced anion-cation pairs (along with water) are able to
20 reside. This likely gives rise to the observed non-zero cation concentration at lower PSS mol
21 fraction. Further, ions entering the crystalline nano fibrillar structures may themselves be in
22 thermodynamic equilibrium with the ions in the voids within the film (in addition to the external
23 electrolyte). Also, ion trapping within the film may also occur to give an increased ionic content.

24 Whether considering the voids and nanofibrillar domains within crys-PEDOT:PSS,^{75, 76} the
25 PEDOT-rich versus PSS-rich domains within EG/GOPS-PEDOT:PSS,²⁶ or the crystalline and
26 amorphous domains in pg2T-TT,⁵⁹ the distribution of ions throughout OMIECs is not necessarily
27 homogenous. In the case of EG/GOPS-PEDOT:PSS, the mesoscale structure is a mixture of
28 PEDOT-rich and PSS-rich domains.²⁶ Thus, passive cation-proton exchange is expected to lead
29 to higher metal cation concentrations within the PSS-rich domains than the PEDOT-rich
30 domains. Semi-crystalline pg2T-TT is presumed to present ordered/crystalline domains

1 embedded in an amorphous matrix, similar to well-studied alkyl-side chain polythiophenes.⁷⁸⁻⁸⁰
2 Spectroscopic studies on closely related alkyl-sidechain materials have been interpreted as
3 indicating a potential-dependent differential distribution of dopant ions between the amorphous
4 and crystalline regions.⁸¹ Thus, to further understand the distribution of ions in OMIEC films, we
5 performed ex situ GISAXS experiments collecting 2-D small angle scattering patterns from films
6 as prepared (neat), after electrolyte exposure, and after electrochemical (re/de)-doping. In
7 GISAXS, the changes in feature positions indicate a change in mesoscale structure on
8 exposure/electrochemical biasing, where as a change in feature intensity decay would be an
9 indicator of changes in electron density associated with ionic/water distributions.

10



11

12 **Figure 5** the in-plane (q_r) linecut of GISAXS patterns in Yoneda region of a) EG/GOPS-
13 PEDOT:PSS, b) pg2T-TT and c) crys-PEDOT:PSS in different doping level.

14

15 2-D ex situ GISAXS patterns were collected for EG/GOPS-PEDOT:PSS films neat/as cast,
16 electrolyte exposed, electrochemically dedoped (-0.6 V vs Ag/AgCl), and electrochemically
17 redoped to a roughly equilibrium oxidation state (0.0 V vs Ag/AgCl) (**Figure S8**). Line-cuts
18 from all the films conditions displayed a similar broad scattering feature between 0.01 and 0.03
19 \AA^{-1} (**Figure 5a**), indicating that mesoscale structure (phase separation of PEDOT-rich and PSS-
20 rich domains) is essentially constant due to high level of crosslinking, with a domain length-scale
21 in keeping with previous investigations.²⁶

22 With ex situ exposed and biased films, the changes in small angle scattering intensity are
23 ascribed to larger changes in cation concentration within the PEDOT-rich domains compared to

1 the PSS-rich matrix.²⁶ The exposed (having undergone proton-cation exchange) and redoped line
2 cuts were nominally identical, which was intuitive as they should both have same cation
3 concentration and distribution. The neat and dedoped line-cuts were nominally identical with
4 each other, and distinct from the exposed and redoped line cuts, with a suppression of the main
5 scattering feature. This reflects a diminished electron density contrast between the PSS-rich and
6 PEDOT-rich domains due to the minimal effect of protons in the cation-free neat film, and the
7 decreased differential cation concentration between the domains in the dedoped samples, as
8 cations displace holes in the PEDOT-rich domains.

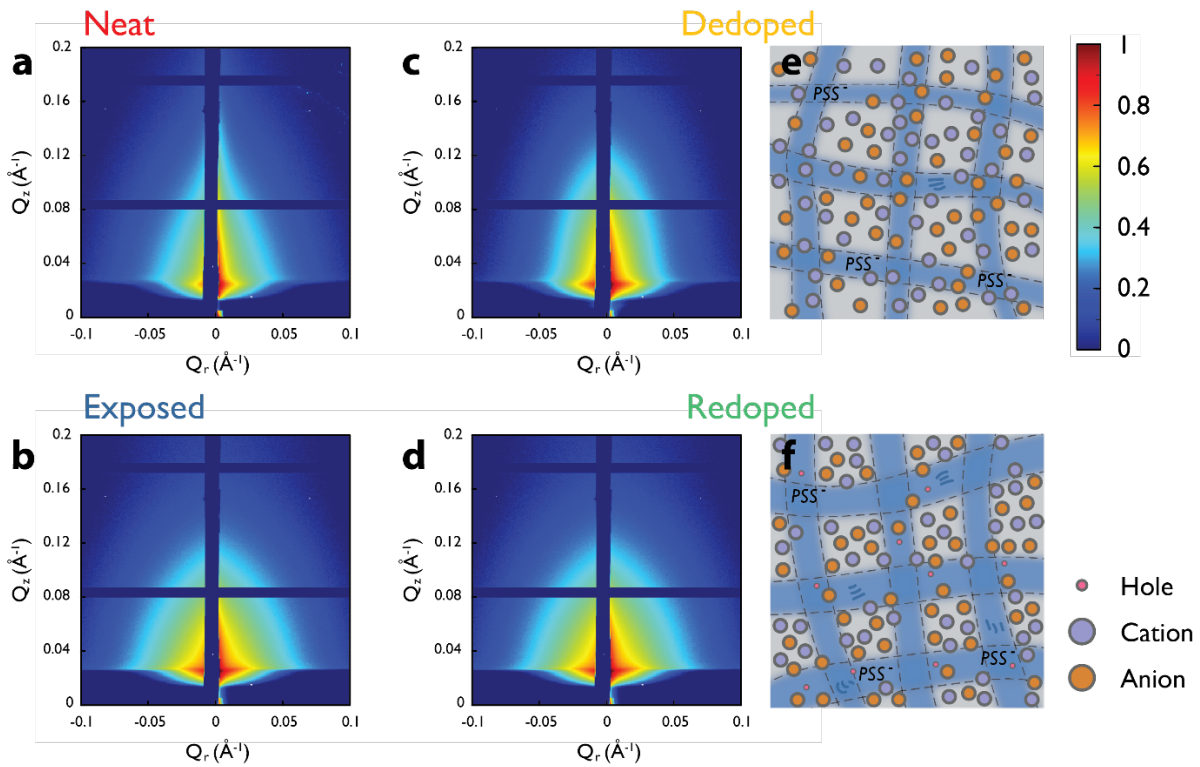
9 GISAXS patterns of pg2T-TT neat, ex situ electrolyte exposed, dedoped (-0.2 V vs Ag/AgCl),
10 and redoped (+0.5 V vs Ag/AgCl) films were also collected (**Figure S9**). Line-cuts from the neat
11 and electrolyte exposed films were nominally identical (**Figure 5b**), implying no mesoscale
12 disruption/reordering and a uniform distribution of passively incorporated ions. This stands in
13 contrast to analogous alkyl sidechain polythiophenes exposed to ionic liquid electrolytes, where
14 ions are presumed to preferentially enter the amorphous domains.⁸¹ Here, a uniform ion uptake in
15 both amorphous and crystalline domains is in keeping with the large lamellar expansions in
16 pg2T-TT upon electrolyte exposure seen with in situ GIWAXS.⁸² It is difficult to rationalize
17 60% lamellar expansion not reflecting significant ion uptake into the intra-lamellar regions of
18 crystalline domains. Compared to the neat and exposed films, line-cuts from ex situ dedoped
19 films displayed a subtle slope increase and intensity decrease, while line-cuts from ex situ
20 redoped films displayed a subtle slope decrease and intensity increase. The relatively minimal
21 scattering differences across conditions implies that passive ion uptake, and potential dependent
22 (de)doping results in relatively uniform changes in ion density within the amorphous and
23 crystalline domains of pg2T-TT in aqueous metal halide electrolytes.

24 In both EG/GOPS-PEDOT:PSS and pg2T-TT, the differences in GISAXS patterns across
25 conditions indicate small morphological changes relative to the mesoscale changes that occur in
26 related conjugated polymer systems during co-deposition,⁸³ in response to changes in humidity,⁸⁴
27 and operation in a thermoelectric²⁵ or photovoltaic devices.⁸⁵

28 In contrast to the subtle changes in small angle scattering in EG/GOPS-PEDOT:PSS and pg2T-
29 TT, crys-PEDOT:PSS showed much larger differences in small angle scattering between ex situ
30 conditions (**Figure 5c**, **Figure 6a-d**). In this case, the conditions were neat (as prepared, **Figure**

1 **6a**), electrolyte exposed (**Figure 6b**), dedoped (-0.6 V vs Ag/AgCl, **Figure 6c**), and redoped to a
 2 high oxidation state (+0.6 V vs Ag/AgCl, **Figure 6d**). As discussed above, sulfuric acid
 3 treatment of PEDOT:PSS removed excess PSS and drove the formation of a crystallized
 4 nanofibrillar structure. Thus, the anticipated possible effects of ex situ electrolyte exposure and
 5 electrochemical (de)doping are differential accumulation of ions within the crystalline nanofibers
 6 and voids, and swelling of the crystalline nanofibers.

7



8 **Figure 6** GISAXS patterns for crys-PEDOT:PSS in a) neat film; b) exposed in 100mM RbBr
 9 solution at pH=7; c) dedoped at -0.6V vs Ag/AgCl in 100mM RbBr solution at pH=7; d) redoped
 10 to a high oxidation state at +0.6V vs Ag/AgCl in 100mM RbBr solution at pH=7; e) schemes for
 11 ion distribution in the neat, dedoped states and f) exposed, redoped states.

13

14 Neat film GISAXS line-cuts displayed a pronounced shoulder around 0.02 \AA^{-1} (**Figure 5c**). This
 15 feature was enhanced and shifted to higher q-vector upon electrolyte exposure, diminished upon
 16 dedoping, and enhanced once again when redoped to a high oxidation state. The resulting

1 exposure/doping dependent scattering intensity trends observed in the mid-q region (q_z between
2 $0.15\text{--}0.2 \text{ \AA}^{-1}$) were consistent intensity trends for the overlapping q-range previously observed
3 with operando GIWAXS.⁴⁵ The normalized intensity contrast is significantly enhanced when
4 crys-PEDOT:PSS is in the doped state (both electrolyte exposed and redoped states, **Figure**
5 **6b&d**), implying a non-uniform ion distribution. With respect to the neat (as prepared) films, in-
6 plane line-cuts from exposed and redoped film GISAXS scattering patterns both displayed an
7 increase in intensity of the scattering feature and a shift to higher q-vector (**Figure 5c**). The
8 intensity increase due to exposure is ascribed to larger electron density contrast between the
9 crystalline nanofibrillar domains and the inter-fibrillar voids/domains arising from
10 inhomogeneous uptake of ions into the film (**Figure 6f**). From ex situ XRF, it is apparent that
11 significant amount of charge balanced anion-cation pairs enters the film, which presumably
12 reside in inter-fibrillar voids/domains. Additionally, ex situ XRF revealed that excess anions also
13 enter the film, (as the equilibrium degree of doping in pH neutral electrolyte is higher than as
14 prepared), and these dopant anions are expected to reside within the nanofibrils to compensate
15 the enhanced hole density. Thus we tentatively interpret the shift to higher q-vector as reflecting
16 a shrinking of the inter-fibrillar voids/domains as the crystalline nanofibrils expand.

17 With respect to the exposed and redoped films, in-plane line-cuts from dedoped film GISAXS
18 scattering patterns displayed a decrease in intensity of the scattering feature and a shift to higher
19 q-vector, bringing it more in line with the as prepared scattering data (**Figure 5c**). The intensity
20 decrease is ascribed to suppression of the electron density contrast between the crystalline
21 nanofibrillar domains and the inter-fibrillar voids/domains due to the ion reorganization (cation
22 accumulation within the nanofibrils) that accompanies dedoping, while the shift to higher q-
23 vector as reflects an expansion of the inter-fibrillar voids/domains as the nanofibrils contract
24 (**Figure 6e**).

25 A Guinier-style analysis of the line-cuts was carried out to provide a semi-quantitative analysis
26 of the relative mesoscale changes (**Figure S10**). From the Guinier-style analysis of the particle
27 size distribution a square weighted average characteristic length scale was obtained (**Table S1**).
28 Again, this length scale is interpreted as representing the size of inter-fibrillar voids/domains
29 embedded in a nanofibrillar mesh. In keeping with our above qualitative analysis, the as cast
30 (neat) and dedoped samples gave similar characteristic length scales, 128 and 132 \AA ,

1 respectively. The exposed and redoped samples were likewise similar, with characteristic length
2 scales of 78.0 and 66.7 Å, respectively. The ~50-65 Å difference between exposed/redoped and
3 neat/dedoped is ascribed to a contraction of the inter-fibrillar void/domain. This inter-fibrillar
4 void/domain contraction is inversely correlated with a crystallite expansion (~12%) previously
5 determined by in situ GIWAXS.⁴⁵ As the acid treatment produces highly crystalline nanofibrils,
6 it is presumed that the nanofibrillar expansion is likely equivalent to the crystallite expansion.

7 It must be noted that ex situ GISAXS probes the dry “collapsed” structure, water (which by
8 EQCM, contributes significantly to swelling) is for the large part absent from the films. What is
9 interpreted in the ex situ films as an inter-fibrillar void/domain contraction may not maintain in
10 situ when the film is swollen with water as well as extra ions. This highlights the need for in
11 situ/operando GISAXS for OMIECs, which is an ongoing effort.

12

13 Conclusion

14 In summary, we quantified the ionic composition of different species of p-type OMIEC after
15 electrolyte exposure and electrochemical cycling. Among them, the presence of polyelectrolyte
16 in OMIEC significantly affects the ionic species involved in the electrochemical cycle. The
17 polyelectrolyte functioned as a buffer and minimized the effect of electrolyte concentration and
18 pH on the changes in OMIEC composition. Specifically, the negatively charged polyelectrolyte
19 PSS⁻ prevents mobile anions from entering the polymer due to Donnan exclusion, where the
20 fixed polyanionic charge repels the uptake of ions with the same sign charge. The passive ion
21 uptake under electrolyte exposure in PEDOT:PSS with different polyelectrolyte contents was
22 simulated by an appropriate Donnan model. The amount of fixed charge controls the strength of
23 Donnan exclusion and thus controls the ultimate film composition. We also analyzed the
24 mesoscale structure and ion distribution using GISAXS, which shows mild ion segregation in the
25 polymer blend EG/GOPS-PEDOT:PSS and little ion segregation in single-component OMIEC
26 pg2T-TT during the electrochemical cycling. In the crys-PEDOT:PSS with a well-defined
27 fibrillar crystalline structure, the doped state of the polymer shows a significant inhomogeneous
28 ion distribution and a contraction of the inter-fibrillar void/domain.

1 The accurate quantification of ionic composition in OMIECs reveals the complexity of ion
 2 transport and charge trapping in their aqueous working conditions. This work highlights the
 3 limitations of assuming that the measured currents in OMIECs correspond solely to the ion flux.
 4 The direct charge transfer via Faradaic reactions causes overestimations of the ion content in the
 5 OMIECs, thus leading to the underestimation of the amount of water accompanying the dopant
 6 ions. Specifically, we show that cation transport into the film is accompanied by more water than
 7 a single ~6 water molecule hydration shell. For the conjugated polymers lacking fixed ionic
 8 charge, this work quantifies the significant amount of ion charge trapping present during
 9 electrochemical cycling. Compared to P3HT lacking hydrophilic side chains,⁸⁶ pg2T-TT exhibits
 10 a larger proportion of irreversible trapping of dopants anions. Key results of this study and the
 11 comparisons to previous work are summarized in **Table 1**. As a non-invasive elemental
 12 quantification technique, XRF is a promising tool for studying ion composition and transport
 13 properties in OMIECs. Achieving *in situ/operando* implementation of this technique will be a
 14 challenge, and this report serves as a foundation for that endeavor.

15 **Table 1** Summary of this work and previous works on OMIEC composition

Technique	Material	Dopant ion modulation per repeat unit	Accompanying water molecules per dopant ion	Ion trapped
This work	EG/GOPS-PEDOT:PSS	0.19	11.6	-
This work	pg2T-TT	0.52	-	34%
This work	crys-PEDOT:PSS	0.08	>100	-
NMR ^{87*}	EG/GOPS-PEDOT:PSS	0.11	-	-
EQCM ¹⁰	EG/GOPS-PEDOT:PSS	-	2-4	-
EQCM ^{11**}	pg2T-TT	0.63	7-9	-
GDOES ¹⁶	P3MEEMT	0.18	-	-
APXPS ⁵⁶	PSSNa	-	8-10	-
UV-Vis ⁸⁶	P3HT	-	-	15-22%

16 *This is an *operando* measurement but in an extremely thick film (0.15mm);

17 **Estimated from the result cycled in 100mM NaCl between 0.5 and 0V vs V_{OCP} .

18

19 **Supporting Information**

1 This supporting information provides the details of the Donnan model and the GISAXS analysis;
2 EQCM data for EG/GOPS-PEDOT:PSS and crys-PEDOT:PSS; extra data for XRF, XPS and
3 GISAXS. (PDF)

4 **Acknowledgements**

5 R.W., B.P., and J.R. gratefully acknowledge support from the National Science Foundation
6 Grant No. NSF DMR-1751308. The synchrotron XRF work was performed at the 5-BM-D
7 beamline of the DuPont-Northwestern-Dow Collaborative Access Team (DND-CAT) located at
8 Sector 5 of the Advanced Photon Source (APS). DND-CAT is supported by Northwestern
9 University, The Dow Chemical Company, and DuPont de Nemours, Inc. GISAXS measurements
10 were performed at beamline 8-ID-E of the APS. The APS is a U.S. Department of Energy (DOE)
11 Office of Science User Facility operated for the DOE Office of Science by Argonne National
12 Laboratory under Contract No. DE-AC02-06CH11357. This research used resources of the
13 Advanced Photon Source; a U.S. Department of Energy (DOE) Office of Science User Facility
14 operated for the DOE Office of Science by Argonne National Laboratory under Contract No.
15 DE-AC02-06CH11357. This work utilized the Keck-II facility of Northwestern University's
16 NUANCE Center, supported by the Soft and Hybrid Nanotechnology Experimental (SHyNE)
17 Resource (NSF ECCS-1542205), the Materials Research Science and Engineering Center (NSF
18 DMR-1720139), the State of Illinois, and Northwestern University. Additionally, the Keck-II
19 facility is partially supported by the International Institute for Nanotechnology (IIN); the Keck
20 Foundation; and the State of Illinois, through the IIN. This work also utilized the IMSERC
21 facility in Northwestern University. IMSERC is funded by NSF CHE-9871268 (1998) and
22 Northwestern University. Special thanks to Maximilian Moser for providing the materials
23 essential to the characterization of this study.

24

25 **Reference**

26 1. Pitsalidis, C.; Pappa, A.-M.; Boys, A. J.; Fu, Y.; Moysidou, C.-M.; Van Niekerk, D.; Saez,
27 J.; Savva, A.; Iandolo, D.; Owens, R. M., Organic Bioelectronics for in Vitro Systems. *Chem.*
28 *Rev.* **2022**, 122(4), 4700-4790.

1 2. Berggren, M.; Głowacki, E. D.; Simon, D. T.; Stavrinidou, E.; Tybrandt, K., In Vivo
2 Organic Bioelectronics for Neuromodulation. *Chem. Rev.* **2022**, *122*(4), 4826-4846.

3 3. Manousiouthakis, E.; Park, J.; Hardy, J. G.; Lee, J. Y.; Schmidt, C. E., Towards the
4 Translation of Electroconductive Organic Materials for Regeneration of Neural Tissues. *Acta*
5 *Biomater.* **2021**, *139*, 22-42.

6 4. Petty, A. J.; Keate, R. L.; Jiang, B.; Ameer, G. A.; Rivnay, J., Conducting Polymers for
7 Tissue Regeneration in Vivo. *Chem. Mater.* **2020**, *32*, 4095-4115.

8 5. Sumdani, M. G.; Islam, M. R.; Yahaya, A. N. A.; Safie, S. I., Recent Advancements in
9 Synthesis, Properties, and Applications of Conductive Polymers for Electrochemical Energy
10 Storage Devices: A Review. *Polym. Eng. Sci.* **2022**, *62*, 269-303.

11 6. Malti, A.; Brooke, R.; Liu, X.; Zhao, D.; Andersson Ersman, P.; Fahlman, M.; Jonsson, M.
12 P.; Berggren, M.; Crispin, X., Freestanding Electrochromic Paper. *J. Mater. Chem. C* **2016**, *4*,
13 9680-9686.

14 7. Zhang, Q.; Tsai, C.-Y.; Li, L.-J.; Liaw, D.-J., Colorless-to-Colorful Switching
15 Electrochromic Polyimides with Very High Contrast Ratio. *Nat. Commun.* **2019**, *10*, 1239.

16 8. Ling, H.; Koutsouras, D. A.; Kazemzadeh, S.; Van De Burgt, Y.; Yan, F.; Gkoupidenis, P.,
17 Electrolyte-Gated Transistors for Synaptic Electronics, Neuromorphic Computing, and
18 Adaptable Biointerfacing. *Appl. Phys. Rev.* **2020**, *7*, 011307.

19 9. Ji, X.; Paulsen, B. D.; Chik, G. K. K.; Wu, R.; Yin, Y.; Chan, P. K. L.; Rivnay, J.,
20 Mimicking Associative Learning Using an Ion-Trapping Non-Volatile Synaptic Organic
21 Electrochemical Transistor. *Nat. Commun.* **2021**, *12*, 2480.

22 10. Savva, A.; Wustoni, S.; Inal, S., Ionic-to-Electronic Coupling Efficiency in PEDOT:PSS
23 Films Operated in Aqueous Electrolytes. *J. Mater. Chem. C* **2018**, *6*, 12023-12030.

24 11. Savva, A.; Cendra, C.; Giugni, A.; Torre, B.; Surgailis, J.; Ohayon, D.; Giovannitti, A.;
25 McCulloch, I.; Di Fabrizio, E.; Salleo, A., et al., Influence of Water on the Performance of
26 Organic Electrochemical Transistors. *Chem. Mater.* **2019**, *31*, 927-937.

27 12. Savva, A.; Ohayon, D.; Surgailis, J.; Paterson, A. F.; Hidalgo, T. C.; Chen, X.; Maria, I.
28 P.; Paulsen, B. D.; Petty, A. J.; Rivnay, J., et al., Solvent Engineering for High-Performance N-
29 Type Organic Electrochemical Transistors. *Adv. Electron. Mater.* **2019**, *5*, 1900249.

1 13. Wang, Y.; Hamidi-Sakr, A.; Surgailis, J.; Zhou, Y.; Liao, H.; Chen, J.; Zhu, G.; Li, Z.;
2 Inal, S.; Yue, W., The Effect of the Donor Moiety of Dpp Based Polymers on the Performance of
3 Organic Electrochemical Transistors. *J. Mater. Chem. C* **2021**, *9*, 13338-13346.

4 14. Szumska, A. A.; Maria, I. P.; Flagg, L. Q.; Savva, A.; Surgailis, J.; Paulsen, B. D.; Moia,
5 D.; Chen, X.; Griggs, S.; Mefford, J. T., et al., Reversible Electrochemical Charging of N-Type
6 Conjugated Polymer Electrodes in Aqueous Electrolytes. *J. Am. Chem. Soc.* **2021**, *143*, 14795-
7 14805.

8 15. Wang, S. Y.; Li, F.; Easley, A. D.; Lutkenhaus, J. L., Real-Time Insight into the Doping
9 Mechanism of Redox-Active Organic Radical Polymers. *Nat. Mater.* **2019**, *18*, 69.

10 16. Flagg, L. Q.; Bischak, C. G.; Quezada, R. J.; Onorato, J. W.; Luscombe, C. K.; Ginger, D.
11 S., P-Type Electrochemical Doping Can Occur by Cation Expulsion in a High-Performing
12 Polymer for Organic Electrochemical Transistors. *ACS Mater. Lett.* **2020**, *2*, 254-260.

13 17. Quill, T. J.; Lecroy, G.; Melianas, A.; Rawlings, D.; Thiburce, Q.; Sheelamanthula, R.;
14 Cheng, C.; Tuchman, Y.; Keene, S. T.; McCulloch, I., et al., Ion Pair Uptake in Ion Gel
15 Devices Based on Organic Mixed Ionic–Electronic Conductors. *Adv. Funct. Mater.* **2021**,
16 2104301.

17 18. Paulsen, B. D.; Tybrandt, K.; Stavrinidou, E.; Rivnay, J., Organic Mixed Ionic–Electronic
18 Conductors. *Nat. Mater.* **2020**, *19*, 13-26.

19 19. Panchuk, V.; Yaroshenko, I.; Legin, A.; Semenov, V.; Kirsanov, D., Application of
20 Chemometric Methods to Xrf-Data - a Tutorial Review. *Anal. Chim. Acta.* **2018**, *1040*, 19-32.

21 20. Vanhoof, C.; Bacon, J. R.; Fittschen, U. E. A.; Vincze, L., 2020 Atomic Spectrometry
22 Update – a Review of Advances in X-Ray Fluorescence Spectrometry and its Special
23 Applications. *J. Anal. At. Spectrom.* **2020**, *35*, 1704-1719.

24 21. Potts, P. J.; Ellis, A. T.; Holmes, M.; Kregsamer, P.; Strelí, C.; West, M.; Wobrauscheck,
25 P., X-Ray Fluorescence Spectrometry. *J. Anal. At. Spectrom.* **2000**, *15*, 1417-1442.

26 22. Nakayama, K.; Nakamura, T., Calibrating Standards Using Chemical Reagents for Glass
27 Bead X-Ray Fluorescence Analyses of Geochemical Samples. *X-Ray Spectrom.* **2008**, *37*, 204-
28 209.

29 23. Sanyal, K.; Chappa, S.; Bahadur, J.; Pandey, A. K.; Mishra, N. L., Arsenic Quantification
30 and Speciation at Trace Levels in Natural Water Samples by Total Reflection X-Ray

1 Fluorescence after Pre-Concentration with N-Methyl-D-Glucamine Functionalized Quartz
2 Supports. *J. Anal. At. Spectrom.* **2020**, *35*, 2770-2778.

3 24. Nikiforov, M. P.; Lai, B.; Chen, W.; Chen, S.; Schaller, R. D.; Strzalka, J.; Maser, J.;
4 Darling, S. B., Detection and Role of Trace Impurities in High-Performance Organic Solar Cells.
5 *Energy Environ. Sci.* **2013**, *6*, 1513.

6 25. Oechsle, A. L.; Heger, J. E.; Li, N.; Yin, S.; Bernstorff, S.; Müller-Buschbaum, P., In Situ
7 Observation of Morphological and Oxidation Level Degradation Processes within Ionic Liquid
8 Post-Treated PEDOT:PSS Thin Films Upon Operation at High Temperatures. *ACS Appl. Mater.*
9 *Interfaces.* **2022**, *14*, 30802-30811.

10 26. Rivnay, J.; Inal, S.; Collins, B. A.; Sessolo, M.; Stavriniou, E.; Strakosas, X.; Tassone,
11 C.; Delongchamp, D. M.; Malliaras, G. G., Structural Control of Mixed Ionic and Electronic
12 Transport in Conducting Polymers. *Nat. Commun.* **2016**, *7*, 11287.

13 27. Palumbiny, C. M.; Schlipf, J.; Hexemer, A.; Wang, C.; Muller-Buschbaum, P., The
14 Morphological Power of Soap: How Surfactants Lower the Sheet Resistance of PEDOT:PSS by
15 Strong Impact on Inner Film Structure and Molecular Interface Orientation. *Adv. Electron.*
16 *Mater.*, **2016**, *2*, 1500377.

17 28. Palumbiny, C. M.; Liu, F.; Russell, T. P.; Hexemer, A.; Wang, C.; Müller-Buschbaum, P.,
18 The Crystallization of PEDOT:PSS Polymeric Electrodes Probed in Situ During Printing. *Adv.*
19 *Mater.* **2015**, *27*, 3391-3397.

20 29. Jiang, X.; Chotard, P.; Luo, K.; Eckmann, F.; Tu, S.; Reus, M. A.; Yin, S.; Reitenbach,
21 J.; Weindl, C. L.; Schwartzkopf, M., et al., Revealing Donor–Acceptor Interaction on the
22 Printed Active Layer Morphology and the Formation Kinetics for Nonfullerene Organic Solar
23 Cells at Ambient Conditions. *Adv. Energy Mater.* **2022**, *12*, 2103977.

24 30. Oechsle, A. L.; Heger, J. E.; Li, N.; Yin, S. S.; Bernstorff, S.; Müller-Buschbaum, P.,
25 Correlation of Thermoelectric Performance, Domain Morphology and Doping Level in
26 PEDOT:PSS Thin Films Post-Treated with Ionic Liquids. *Macromol. Rapid. Comm.*, **2021**, *42*,
27 2100397.

28 31. Tu, S.; Tian, T.; Oechsle, A. L.; Yin, S. S.; Jiang, X. Y.; Cao, W.; Li, N.; Scheel, M. A.;
29 Reb, L. K.; Hou, S. J.; Bandarenka, A. S.; Schwartzkopf, M.; Roth, S. V.; Müller-Buschbaum,
30 P., Improvement of the thermoelectric properties of PEDOT:PSS films via DMSO addition and
31 DMSO/salt post-treatment resolved from a fundamental view. *Chem. Eng. J.*, **2022**, *429*, 132295.

1 32. Mohl, G. E.; Metwalli, E.; Muller-Buschbaum, P., In Operando Small-Angle X-Ray
2 Scattering Investigation of Nanostructured Polymer Electrolyte for Lithium-Ion Batteries. *ACS*
3 *Energy Lett.* **2018**, *3*, 1525-1530.

4 33. Galluzzo, M. D.; Grundy, L. S.; Takacs, C. J.; Cao, C. T.; Steinriick, H. G.; Fu, S.;
5 Valadez, M. A. R.; Toney, M. F.; Balsara, N. P., Orientation-Dependent Distortion of Lamellae
6 in a Block Copolymer Electrolyte under Dc Polarization. *Macromolecules* **2021**, *54*, 7808-7821.

7 34. Wu, R.; Paulsen, B. D.; Ma, Q.; Rivnay, J., Mass and Charge Transport Kinetics in an
8 Organic Mixed Ionic-Electronic Conductor. *Chem. Mater.* **2022**, *34*, 9699–9710

9 35. Ouyang, B. Y.; Chi, C. W.; Chen, F. C.; Xi, Q. F.; Yang, Y., High-Conductivity Poly (3,4-
10 Ethylenedioxythiophene): Poly(Styrene Sulfonate) Film and its Application in Polymer
11 Optoelectronic Devices. *Adv. Funct. Mater.* **2005**, *15*, 203-208.

12 36. Takano, T.; Masunaga, H.; Fujiwara, A.; Okuzaki, H.; Sasaki, T., PEDOT Nanocrystal in
13 Highly Conductive PEDOT:PSS Polymer Films. *Macromolecules* **2012**, *45*, 3859-3865.

14 37. Palumbiny, C. M.; Heller, C.; Schaffer, C. J.; Korstgens, V.; Santoro, G.; Roth, S. V.;
15 Muller-Buschbaum, P., Molecular Reorientation and Structural Changes in Cosolvent-Treated
16 Highly Conductive PEDOT:PSS Electrodes for Flexible Indium Tin Oxide-Free Organic
17 Electronics. *J. Phys. Chem. C* **2014**, *118*, 13598-13606.

18 38. Stavriniidou, E.; Leleux, P.; Rajaona, H.; Khodagholy, D.; Rivnay, J.; Lindau, M.; Sanaur,
19 S.; Malliaras, G. G., Direct Measurement of Ion Mobility in a Conducting Polymer. *Adv. Mater.*
20 **2013**, *25*, 4488-4493.

21 39. Berezhetska, O.; Liberelle, B.; De Crescenzo, G.; Cicoira, F., A Simple Approach for
22 Protein Covalent Grafting on Conducting Polymer Films. *J. Mater. Chem. B* **2015**, *3*, 5087-5094.

23 40. Lee, Y. Y.; Choi, G. M.; Lim, S. M.; Cho, J. Y.; Choi, I. S.; Nam, K. T.; Joo, Y. C.,
24 Growth Mechanism of Strain-Dependent Morphological Change in PEDOT:PSS Films. *Sci. Rep-
UK* **2016**, *6*, 25332.

25 41. Khan, M. A.; Armes, S. P.; Perruchot, C.; Ouamara, H.; Chehimi, M. M.; Greaves, S. J.;
26 Watts, J. F., Surface Characterization of Poly(3,4-Ethylenedioxythiophene)-Coated Latexes by
27 X-Ray Photoelectron Spectroscopy. *Langmuir* **2000**, *16*, 4171-4179.

28 42. Im, S. G.; Gleason, K. K.; Olivetti, E. A., Doping Level and Work Function Control in
29 Oxidative Chemical Vapor Deposited Poly (3,4-Ethylenedioxythiophene). *Appl. Phys. Lett.*
30 **2007**, *90*, 152112.

1 43. Taouil, A. E.; Lallemand, F.; Hihn, J. Y.; Melot, J. M.; Blondeau-Patissier, V.; Lakard, B.,
2 Doping Properties of PEDOT Films Electrosynthesized under High Frequency Ultrasound
3 Irradiation. *Ultrason. Sonochem.* **2011**, *18*, 140-148.

4 44. Kim, D.; Zozoulenko, I., Why Is Pristine PEDOT Oxidized to 33%? A Density Functional
5 Theory Study of Oxidative Polymerization Mechanism. *J. Phys. Chem. B* **2019**, *123*, 5160-5167.

6 45. Paulsen, B. D.; Wu, R.; Takacs, C. J.; Steinruck, H. G.; Strzalka, J.; Zhang, Q.; Toney, M. F.; Rivnay, J., Time-Resolved Structural Kinetics of an Organic Mixed Ionic-Electronic
7 Conductor. *Adv. Mater.* **2020**, *32*, 2003404.

9 46. Volkov, A. V.; Wijeratne, K.; Mitraka, E.; Ail, U.; Zhao, D.; Tybrandt, K.; Andreasen, J.
10 W.; Berggren, M.; Crispin, X.; Zozoulenko, I. V., Understanding the Capacitance of
11 PEDOT:PSS. *Adv. Funct. Mater.* **2017**, *27*, 1700329.

12 47. Ling, H.; Liu, L.; Lee, P. S.; Mandler, D.; Lu, X. H., Layer-by-Layer Assembly of
13 PEDOT:PSS and Wo₃ Nanoparticles: Enhanced Electrochromic Coloration Efficiency and
14 Mechanism Studies by Scanning Electrochemical Microscopy. *Electrochim. Acta* **2015**, *174*, 57-
15 65.

16 48. Carli, S.; Di Lauro, M.; Bianchi, M.; Murgia, M.; De Salvo, A.; Prato, M.; Fadiga, L.;
17 Biscarini, F., Water-Based PEDOT:Nafion Dispersion for Organic Bioelectronics. *ACS Appl.
18 Mater. Inter.* **2020**, *12*, 29807-29817.

19 49. Stavriniidou, E.; Sessolo, M.; Winther-Jensen, B.; Sanaur, S.; Malliaras, G. G., A Physical
20 Interpretation of Impedance at Conducting Polymer/Electrolyte Junctions. *AIP Adv.* **2014**, *4*,
21 017127.

22 50. Stavriniidou, E.; Leleux, P.; Rajaona, H.; Fiocchi, M.; Sanaur, S.; Malliaras, G. G., A
23 Simple Model for Ion Injection and Transport in Conducting Polymers. *J. Appl. Phys.* **2013**, *113*,
24 244501.

25 51. Giovannitti, A.; Rashid, R. B.; Thiburce, Q.; Paulsen, B. D.; Cendra, C.; Thorley, K.;
26 Moia, D.; Mefford, J. T.; Hanifi, D.; Du, W. Y., et al., Energetic Control of Redox-Active
27 Polymers toward Safe Organic Bioelectronic Materials. *Adv. Mater.* **2020**, *32*, 1908047.

28 52. Schafer, E. A.; Wu, R. H.; Meli, D.; Tropp, J.; Moser, M.; McCulloch, I.; Paulsen, B. D.;
29 Rivnay, J., Sources and Mechanism of Degradation in P-Type Thiophene-Based Organic
30 Electrochemical Transistors. *ACS Appl. Electron Mater.* **2022**, *4*, 1391-1404.

1 53. Mitraka, E.; Gryszel, M.; Vagin, M.; Jafari, M. J.; Singh, A.; Warczak, M.; Mitrakas, M.;
2 Berggren, M.; Ederth, T.; Zozoulenko, I., et al., Electrocatalytic Production of Hydrogen
3 Peroxide with Poly(3,4-Ethylenedioxothiophene) Electrodes. *Adv. Sustain. Syst.* **2019**, *3*,
4 1800110.

5 54. Kulkarni, A.; Siahrostami, S.; Patel, A.; Norskov, J. K., Understanding Catalytic Activity
6 Trends in the Oxygen Reduction Reaction. *Chem. Rev.* **2018**, *118*, 2302-2312.

7 55. Singh, S. K.; Crispin, X.; Zozoulenko, I. V., Oxygen Reduction Reaction in Conducting
8 Polymer PEDOT: Density Functional Theory Study. *J. Phys. Chem. C* **2017**, *121*, 12270-12277.

9 56. Gokturk, P. A.; Barry, M.; Segalman, R.; Crumlin, E. J., Directly Probing Polymer Thin
10 Film Chemistry and Counterion Influence on Water Sorption. *ACS Appl. Polym. Mater.* **2020**, *2*,
11 4752-4761.

12 57. Fulton, J. L.; Pfund, D. M.; Wallen, S. L.; Newville, M.; Stern, E. A.; Ma, Y. J., Rubidium
13 Ion Hydration in Ambient and Supercritical Water. *J. Chem. Phys.* **1996**, *105*, 2161-2166.

14 58. Galib, M.; Baer, M. D.; Skinner, L. B.; Mundy, C. J.; Huthwelker, T.; Schenter, G. K.;
15 Benmore, C. J.; Govind, N.; Fulton, J. L., Revisiting the Hydration Structure of Aqueous Na^+ . *J.*
16 *Chem. Phys.* **2017**, *146*, 084504.

17 59. Giovannitti, A.; Sbircea, D. T.; Inal, S.; Nielsen, C. B.; Bandiello, E.; Hanifi, D. A.;
18 Sessolo, M.; Malliaras, G. G.; McCulloch, I.; Rivnay, J., Controlling the Mode of Operation of
19 Organic Transistors through Side-Chain Engineering. *P. Natl. Acad. Sci. USA* **2016**, *113*, 12017-
20 12022.

21 60. Giovannitti, A.; Maria, I. P.; Hanifi, D.; Donahue, M. J.; Bryant, D.; Barth, K. J.;
22 Makdah, B. E.; Savva, A.; Moia, D.; Zetek, M., et al., The Role of the Side Chain on the
23 Performance of N-Type Conjugated Polymers in Aqueous Electrolytes. *Chem. Mater.* **2018**, *30*,
24 2945-2953.

25 61. Bronstein, H.; Nielsen, C. B.; Schroeder, B. C.; McCulloch, I., The Role of Chemical
26 Design in the Performance of Organic Semiconductors. *Nat. Rev. Chem.* **2020**, *4*, 66-77.

27 62. Venkatraman, V.; Friedlein, J. T.; Giovannitti, A.; Maria, I. P.; McCulloch, I.; McLeod,
28 R. R.; Rivnay, J., Subthreshold Operation of Organic Electrochemical Transistors for Biosignal
29 Amplification. *Adv. Sci.* **2018**, *5*, 1800453.

1 63. Tan, S. T. M.; Giovannitti, A.; Marks, A.; Moser, M.; Quill, T. J.; McCulloch, I.; Salleo,
2 A.; Bonacchini, G. E., Conjugated Polymers for Microwave Applications: Untethered Sensing
3 Platforms and Multifunctional Devices. *Adv. Mater.* **2022**, 2202994.

4 64. Liang, Z. Q.; Nardes, A.; Wang, D.; Berry, J. J.; Gregg, B. A., Defect Engineering in Pi-
5 Conjugated Polymers. *Chem. Mater.* **2009**, 21, 4914-4919.

6 65. Jiang, M. C.; Yuan, J. F.; Cao, G. Z.; Tian, J. J., In-Situ Fabrication of P3HT Passivating
7 Layer with Hole Extraction Ability for Enhanced Performance of Perovskite Solar Cell. *Chem.*
8 *Eng. J.* **2020**, 402, 126152.

9 66. Li, M. H.; Shao, J. Y.; Jiang, Y.; Qiu, F. Z.; Wang, S.; Zhang, J.; Han, G.; Tang, J.;
10 Wang, F.; Wei, Z., et al., Electrical Loss Management by Molecularly Manipulating Dopant-
11 Free Poly(3-Hexylthiophene) Towards 16.93 % Cspbi 2 Br Solar Cells. *Angew. Chem.* **2021**,
12 133, 16524-16529.

13 67. Li, N.; Feng, A. B.; Guo, X. B.; Wu, J. M.; Xie, S. D.; Lin, Q. L.; Jiang, X. M.; Liu, Y.;
14 Chen, Z. L.; Tao, X. T., Engineering the Hole Extraction Interface Enables Single-Crystal
15 Mapbi(3) Perovskite Solar Cells with Efficiency Exceeding 22% and Superior Indoor Response.
16 *Adv. Energy. Mater.* **2022**, 12, 2103241.

17 68. Xie, H. X.; Liu, J.; Yin, X. T.; Guo, Y. X.; Liu, D.; Wang, G. F.; Que, W. X.,
18 Perovskite/P3HT Graded Heterojunction by an Additive-Assisted Method for High-Efficiency
19 Perovskite Solar Cells with Carbon Electrodes. *Colloid Surface A* **2022**, 635, 128072.

20 69. Muntasir, T.; Chaudhary, S., Understanding Defect Distributions in Polythiophenes via
21 Comparison of Regioregular and Regiorandom Species. *J. Appl. Phys.* **2015**, 118, 205504.

22 70. Arvind, M.; Tait, C. E.; Guerrini, M.; Krumland, J.; Valencia, A. M.; Cocchi, C.;
23 Mansour, A. E.; Koch, N.; Barlow, S.; Marder, S. R., et al., Quantitative Analysis of Doping-
24 Induced Polarons and Charge-Transfer Complexes of Poly(3-Hexylthiophene) in Solution. *J.*
25 *Phys. Chem. B* **2020**, 124, 7694-7708.

26 71. Suppes, G.; Ballard, E.; Holdcroft, S., Aqueous Photocathode Activity of Regioregular
27 Poly(3-Hexylthiophene). *Polym. Chem-UK* **2013**, 4, 5345-5350.

28 72. Kwon, S.; Yu, K.; Kweon, K.; Kim, G.; Kim, J.; Kim, H.; Jo, Y. R.; Kim, B. J.; Kim, J.;
29 Lee, S. H., et al., Template-Mediated Nano-Crystallite Networks in Semiconducting Polymers.
30 *Nat. Commun.* **2014**, 5, 4183.

1 73. Nurazzi, N. M.; Abdullah, N.; Demon, S. Z. N.; Halim, N. A.; Mohamad, I. S., The
2 Influence of Reaction Time on Non-Covalent Functionalisation of P3HT/Mwcnt
3 Nanocomposites. *Polymers-Basel* **2021**, *13*, 1916.

4 74. Kim, Y.; Noh, H.; Paulsen, B. D.; Kim, J.; Jo, I. Y.; Ahn, H.; Rivnay, J.; Yoon, M. H.,
5 Strain-Engineering Induced Anisotropic Crystallite Orientation and Maximized Carrier Mobility
6 for High-Performance Microfiber-Based Organic Bioelectronic Devices. *Adv. Mater.* **2021**, *33*,
7 2007550.

8 75. Kim, S.-M.; Kim, C.-H.; Kim, Y.; Kim, N.; Lee, W.-J.; Lee, E.-H.; Kim, D.; Park, S.;
9 Lee, K.; Rivnay, J., et al., Influence of PEDOT:PSS Crystallinity and Composition on
10 Electrochemical Transistor Performance and Long-Term Stability. *Nat. Commun.* **2018**, *9*, 3858.

11 76. Kim, N.; Kee, S.; Lee, S. H.; Lee, B. H.; Kahng, Y. H.; Jo, Y.-R.; Kim, B.-J.; Lee, K.,
12 Highly Conductive PEDOT:PSS Nanofibrils Induced by Solution-Processed Crystallization. *Adv.*
13 *Mater.* **2014**, *26*, 2268-2272.

14 77. Bae, E. J.; Kang, Y. H.; Jang, K. S.; Cho, S. Y., Enhancement of Thermoelectric Properties
15 of PEDOT:PSS and Tellurium-PEDOT:PSS Hybrid Composites by Simple Chemical Treatment.
16 *Sci. Rep-UK* **2016**, *6*, 18805.

17 78. Collins, B. A.; Cochran, J. E.; Yan, H.; Gann, E.; Hub, C.; Fink, R.; Wang, C.;
18 Schuettfort, T.; McNeill, C. R.; Chabinyc, M. L., et al., Polarized X-Ray Scattering Reveals
19 Non-Crystalline Orientational Ordering in Organic Films. *Nat. Mater.* **2012**, *11*, 536-543.

20 79. Newbloom, G. M.; Kim, F. S.; Jenekhe, S. A.; Pozzo, D. C., Mesoscale Morphology and
21 Charge Transport in Colloidal Networks of Poly(3-Hexylthiophene). *Macromolecules* **2011**, *44*,
22 3801-3809.

23 80. Chen, C.-Y.; Chan, S.-H.; Li, J.-Y.; Wu, K.-H.; Chen, H.-L.; Chen, J.-H.; Huang, W.-Y.;
24 Chen, S.-A., Formation and Thermally-Induced Disruption of Nanowhiskers in Poly(3-
25 Hexylthiophene)/Xylene Gel Studied by Small-Angle X-Ray Scattering. *Macromolecules* **2010**,
26 *43*, 7305-7311.

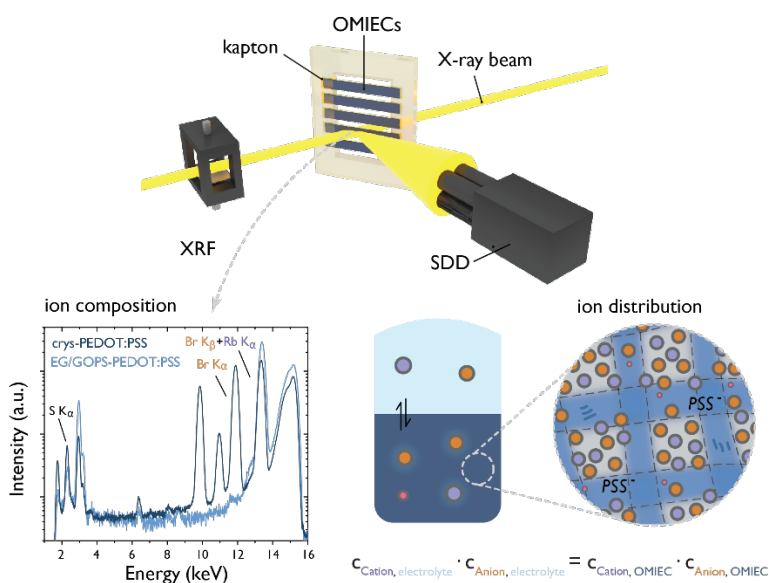
27 81. Thomas, E. M.; Brady, M. A.; Nakayama, H.; Popere, B. C.; Segalman, R. A.; Chabinyc,
28 M. L., X-Ray Scattering Reveals Ion-Induced Microstructural Changes During Electrochemical
29 Gating of Poly(3-Hexylthiophene). *Adv. Funct. Mater.* **2018**, *28*, 1803687.

30 82. Paulsen, B. D.; Giovannitti, A.; Wu, R.; Strzalka, J.; Zhang, Q.; Rivnay, J.; Takacs, C. J.,
31 Electrochemistry of Thin Films with in Situ/Operando Grazing Incidence X-Ray Scattering:

1 Bypassing Electrolyte Scattering for High Fidelity Time Resolved Studies. *Small* **2021**, *17*,
 2 2103213.
 3 83. Proller, S.; Liu, F.; Zhu, C. H.; Wang, C.; Russell, T. P.; Hexemer, A.; Muller-
 4 Buschbaum, P.; Herzig, E. M., Following the Morphology Formation in Situ in Printed Active
 5 Layers for Organic Solar Cells. *Adv. Energy. Mater.* **2016**, *6*, 1501580.
 6 84. Biessmann, L.; Kreuzer, L. P.; Widmann, T.; Hohn, N.; Moulin, J. F.; Muller-Buschbaum,
 7 P., Monitoring the Swelling Behavior of PEDOT:PSS Electrodes under High Humidity
 8 Conditions. *ACS Appl. Mater. Inter.* **2018**, *10*, 9865-9872.
 9 85. Schaffer, C. J.; Palumbiny, C. M.; Niedermeier, M. A.; Burger, C.; Santoro, G.; Roth, S.
 10 V.; Muller-Buschbaum, P., Morphological Degradation in Low Bandgap Polymer Solar Cells -
 11 an in Operando Study. *Adv. Energy. Mater.* **2016**, *6*, 1600712.
 12 86. Hornberger, L. S.; Neusser, D.; Malacrida, C.; Kaake, L. G.; Ludwigs, S., How charge
 13 trapping affects the conductivity of electrochemically doped poly(3-hexylthiophene) films. *Appl.*
 14 *Phys. Lett.* **2021**, *119*, 163301.
 15 87. Lyu, D.; Jin, Y. T.; Magusin, P. C. M. M.; Sturniolo, S.; Zhao, E. W.; Yamamoto, S.;
 16 Keene, S. T.; Malliaras, G. G.; Grey, C. P., Operando NMR electrochemical gating studies of
 17 ion dynamics in PEDOT:PSS. *Nat. Mater.* **2023**.

18

19 **Table Of Contents**



20